Astronomy & Astrophysics manuscript no. ms
February 19, 2026

Gas Accretion versus BH Merger driven Growth Modes of Supermassive Black Holes and Implications for the Little Red Dots

Paramita Barai[1,2,3] ⋆

[1] Istituto Nazionale di Astrofisica (INAF) - Osservatorio Astronomico di Trieste (OATs), Via G.B. Tiepolo 11, I-34143 Trieste, Italy
[2]Centro de Ciências Naturais e Humanas - Universidade Federal do ABC, Av. dos Estados 5001, Santo André - SP, 09210-580, Brazil
[3]Núcleo de Astrofísica - Universidade Cidade de São Paulo, Rua Galvão Bueno 868, São Paulo - SP, 01506-000, Brazil

February 19, 2026

ABSTRACT

We investigate the growth of central supermassive black holes in galaxies, aiming to distinguish between gas accretion versus BH merger-driven growth modes. By performing and analysing cosmological hydrodynamical simulations of $(50\ \mathrm{Mpc})^3$ comoving boxes, we also study how the BH feedback parameters affect the coevolution between SMBHs and their host galaxies. Starting as $10^5 M_\odot$ seeds, we find that the BHs grow initially via BH mergers to $\sim 10^7 M_\odot$. Gas accretion onto the BHs is initially low, then increases with time, and reaches the Eddington rate after 7 – 9 Gyrs. The BHs then undergo very fast growth via efficient gas accretion over a period of 600 – 700 Myr, when the BH mass increases $10^2 - 10^3$ times, causing their predominant growth from $10^7 M_\odot$ to $(10^9 - 10^{10}) M_\odot$. Taking into account the cosmological gas inflows and outflows, SMBHs do not grow to more than $10^{10} M_\odot$ by $z = 0$, because of gas depletion from galaxy centers driven by AGN feedback. In terms of SMBH - host galaxy coevolution along the $M_{\rm BH} - M_\star$ relation, we find that they initially lie below and thereby move upward toward the relation. We make some physical implications of the growth of high-z Little Red Dots recently observed by JWST: the normal-mass SMBHs had predominantly undergone BH merger driven evolution, whereas the overmassive BHs underwent periods of Eddington-limited or super-Eddington bursts of gas accretion.

Key words. cosmological hydrodynamical simulations – supermassive black holes – black hole galaxy coevolution

1. Introduction

Supermassive Black Holes (SMBHs) exist at the centers of active galactic nuclei (AGN), which liberate enormous amounts of feedback energy powered by the accretion of matter (e.g., Rees 1984; Urry & Padovani 1995). AGN are widely observed via multi-wavelength observations, starting from the local Universe up to 13.2 Gyr ago (e.g., Fan et al. 2023; Natarajan et al. 2024). SMBHs already grown to mass $\geq 10^9 M_\odot$ are observed in luminous quasars at $z \sim 6$, when the Universe was less than 1 Gyr old (e.g., Willott et al. 2003; Yang et al. 2023).

How the SMBHs in AGN grew to billions of solar masses involves unresolved questions, despite progress in understanding the SMBH accretion and feedback on the environment (e.g., Alexander et al. 2025). Especially at early epochs, it is difficult to understand how they formed over such short time-scales, and there are open issues with various plausible scenarios (e.g., Dijkstra et al. 2008; Inayoshi & Omukai 2012; Matsumoto et al. 2015). Some studies advocate growth from stellar-mass BHs by rapid enhanced super-Eddington accretion, formation of direct-collapse massive $10^5 M_\odot$ BH seeds soon after the Big Bang (e.g., Volonteri & Rees 2005), via mergers of intermediate-mass black holes (e.g., Barai & de Gouveia Dal Pino 2019).

Adding to the population of early SMBHs, recent JWST observations are revealing $10^7 - 10^8 M_\odot$ BHs at $z \sim 8 - 12$ (e.g., Kokorev et al. 2023; Kocevski et al. 2025; Bhatt et al. 2024; Scholtz et al. 2025). Some of these first SMBHs are overmassive in their host galaxy with respect to the $z = 0$ SMBH-to-stellar mass correlation (e.g., Goulding et al. 2023; Maiolino et al. 2024; Wu et al. 2025). At the same time, a population of normal-mass central SMBHs (with the mean SMBH-to-stellar mass ratio of $\sim 0.1\%$, consistent with the local relation) have been detected in $z \sim 3 - 6$ AGN (e.g., Li et al. 2025; Geris et al. 2025) observed by JWST.

The formation channels of these "normal-mass" and overmassive SMBHs, in terms heavy seeds or super-Eddington accretion onto lighter stellar-mass seeds, have not been identified yet (e.g. Jeon et al. 2025). The very existence of such normal SMBHs together with the overmassive population, imply that there might be diverse pathways for SMBH formation.

Using SDSS/Subaru data, Li et al. (2021) found no significant evolution of the $M_{\rm BH} - M_\star$ relation of quasars between $z = 0.8 - 0.2$, and it remains consistent with the local relation. Graham et al. (2025) argue that the $M_{\rm BH}/M_\star$ correlation that a population of galaxies (including the JWST detected high-z little red dots) follows, is dependent on galaxy morphology. Also using JWST observations, Juodzbalis et al. (2025) detected low-luminosity AGN at $z = 1.5 - 9$, accreting at likely sub-Eddington ratios, hosted in low mass ($M_\star \sim 10^8 M_\odot$) galaxies; where the SMBHs are overmassive relative to the local $[M_{\rm BH} - M_\star]$ relation, while consistent with the local $[M_{\rm BH} - \sigma_\star]$ relation.

Numerical simulations have advanced in parallel to understand these SMBH evolution. Concordance galaxy formation models based on cold dark-matter cosmology widely invoke AGN feedback as a crucial ingredient to self-regulate galaxy and SMBH growth. This has been studied in numerical hydrodynamical simulations (e.g., Di Matteo et al. 2005; Ostriker et al. 2010; Barai et al. 2011; Khandai et al. 2015; Dubois et al. 2016), as well as semi-analytical models (e.g., Kauffmann & Haehnelt 2000; Somerville et al. 2008; Fontanot et al. 2020).

⋆ paramita.barai@inaf.it

Related to the goals of our study, Habouzit et al. (2022) showed that the Illustris, TNG100, TNG300, Horizon-AGN, EAGLE, and SIMBA cosmological simulations do not agree on whether BHs at $z > 4$ are overmassive or undermassive with respect to the $M_{\rm BH} - M_\star$ scaling relation at $z = 0$. Haidar et al. (2022) investigated AGN populations in the Illustris, TNG, Horizon-AGN, EAGLE, and SIMBA simulations compared with current observational constraints in low-mass galaxies, finding that some simulations produce BHs that are too massive. Using (18 Mpc)^3 simulations, Kho et al. (2025) found that different BH seeding models lead to different normalizations of the $M_{\rm BH} - \sigma$ relation. Kho et al. (2025) also found that the BH growth is merger-dominated in low-mass ($\leq 10^9 M_\odot$) galaxies, and is accretion dominated in high-mass ($\geq 10^9 M_\odot$) galaxies; which directly influences the $M_{\rm BH} - \sigma$ evolution.

In our study, we investigate the growth of central SMBHs versus their host galaxies, by performing (50 Mpc)^3 cosmological hydrodynamical simulations, aiming to distinguish between gas accretion versus BH merger-driven growth modes. We probe the SMBH-galaxy coevolution, in particular that of the black hole mass - stellar mass correlation. We also shed light on the growth modes of the overmassive versus normal-mass SMBHs in high-z little red dots recently observed by JWST.

2. Methodology

We perform (50 Mpc)^3 cosmological hydrodynamical simulations, using a modified version of the code GADGET-3 (Springel 2005). The code uses the Tree-PM (particle mesh) and SPH (smoothed particle hydrodynamics) methods. The baryonic physical processes occurring in the multiphase interstellar medium (ISM), on scales unresolved in cosmological simulations, is modeled using spatially averaged properties describing the medium on scales that are resolved, as described in §2.1 and §2.2. Our different simulation runs are outlined in §2.3.

2.1. Cooling, Star-Formation, SN Feedback

Radiative cooling and heating is implemented, including metal-line cooling (Wiersma et al. 2009). In this model, net cooling rates are computed element-by-element tracking 11 atomic species: H, He, C, Ca, O, N, Ne, Mg, S, Si, Fe. A spatially-uniform time-dependent photoionizing background radiation is considered from the cosmic microwave background and the Haardt & Madau (2001) model for the ultraviolet/X-ray background. The gas is assumed to be dust free, optically thin, and in (photo-) ionization equilibrium. Contributions from the 11 elements are interpolated as a function of density, temperature and redshift from tables that have been pre-computed using the public photoionization code CLOUDY (last described by Ferland et al. 1998).

Star formation (SF) is adopted following the multiphase effective sub-resolution model of Springel & Hernquist (2003). Gas particles with density above a limiting threshold, $\rho_{\rm SF} = 0.13$ cm^{-3} (in units of number density of hydrogen atoms), represent cold and hot phase regions of the ISM. Stellar evolution and chemical enrichment are computed for the 11 elements (Tornatore et al. 2007). Each star particle is treated as a simple stellar population (SSP). Given a stellar initial mass function (IMF), the mass of the SSP is varied in time following the death of stars, and accounting for stellar mass losses. A fixed stellar initial mass function (Chabrier 2003) is included, in the mass range $(0.1 - 100)M_\odot$. Stars within a mass interval $[8 - 40]M_\odot$ become SN first before turning into stellar-mass black holes at the end of their lives, while stars of mass $> 40M_\odot$ are allowed to directly end in black holes without contributing to gas enrichment.

Feedback from supernovae is incorporated in the kinetic form, assuming a mass ejection rate $\dot{M}_{\rm SN}$ proportional to the star formation rate ($\dot{M}_\star$):

$$\dot{M}_{\rm SN} = \eta \dot{M}_\star. \quad (1)$$

The mass loading factor of SN wind is taken as $\eta = 2$ (e.g., Tornatore et al. 2007; Barai et al. 2013; Melioli et al. 2013), following observations revealing that SN-driven outflow rates are comparable to or larger than SF rates of galaxies (e.g., Martin 1999; Bouché et al. 2012). The SN wind kinetic power is a fixed fraction χ of SN internal energy rate:

$$\frac{1}{2}\dot{M}_{\rm SN} v_{\rm SN}^2 = \chi \epsilon_{SN} \dot{M}_\star. \quad (2)$$

Here $v_{\rm SN}$ is the SN wind velocity, ϵ_{SN} is the average energy released by SN for each $M_\odot$ of stars formed under the instantaneous recycling approximation. For our adopted Chabrier (2003) power-law IMF, $\epsilon_{SN} = 1.1 \times 10^{49}$ erg $M_\odot^{-1}$. Combining above expressions, $v_{\rm SN}$ can be re-written as: $v_{\rm SN} = (2\chi\epsilon_{SN}/\eta)^{1/2}$. Following a series of studies (e.g., Tornatore et al. 2007; Tescari et al. 2011; Barai et al. 2013), and unlike (Springel & Hernquist 2003), we choose $v_{\rm SN}$ as a free parameter. We adopt a constant-velocity outflow with SN wind velocity $v_{\rm SN} = 350$ km/s (as was done in e.g. Tornatore et al. 2007; Barai et al. 2015; Biffi et al. 2016). Bondi accretion boost factor, $\alpha_{\rm B} = 0.4$.

2.2. BH Accretion and Feedback

We identify galaxies in our simulations by executing the FOF at time intervals of a multiplicative factor 1.4 of the cosmological scale factor a, or, $a_{\rm next}/a_{\rm prev} = 1.4$. Massive galaxies with (i) a total halo mass higher than $10^{10} M_\odot$, (ii) a stellar mass higher than $5 \times 10^7 M_\odot$, (iii) the gas mass is equal or larger than 10 percent of stellar mass, (iv) not containing a BH yet, are selected. A BH of initial mass $M_{\rm BH} = 10^5 M_\odot$ is seeded at the center of each such massive halo.

Gas is considered to accrete onto a BH according to the Bondi-Hoyle-Lyttleton accretion rate ($\dot{M}_{\rm Bondi}$: Bondi 1952),

$$\dot{M}_{\rm Bondi} = \alpha_{\rm B} \frac{4\pi G^2 M_{\rm BH}^2 \rho}{(c_s^2 + v^2)^{3/2}}, \quad (3)$$

where G is the gravitational constant, c_s is the sound speed, ρ is the gas density, v is the velocity of the BH relative to the gas, and $\alpha = 100$ is a numerical boost factor (e.g., Springel et al. 2005; Johansson et al. 2008; Dubois et al. 2013). Furthermore, accretion is limited to the Eddington mass accretion rate ($\dot{M}_{\rm Edd}$): $\dot{M}_{\rm BH} = \min\left(\dot{M}_{\rm Bondi}, \dot{M}_{\rm Edd}\right)$. The Eddington luminosity is used to express the Eddington mass accretion rate,

$$L_{\rm Edd} = \frac{4\pi G M_{\rm BH} m_p c}{\sigma_T} = \epsilon_r \dot{M}_{\rm Edd} c^2, \quad (4)$$

where m_p is the mass of a proton, c is the speed of light, and σ_T is the Thomson scattering cross-section for an electron.

Feedback energy is distributed to the surrounding gas, according to:

$$\dot{E}_{\rm feed} = \epsilon_f \epsilon_r \dot{M}_{\rm BH} c^2. \quad (5)$$

Table 1: Simulation runs and parameter values changed in each case.

Run name	BH present	Seed BH mass, $M_{\rm BHseed}[M_\odot]$	BH feedback efficiency ϵ_f	Type of BH feedback	BH kinetic feedback kick velocity v_w (km/s)
SFonly	–	–	–	–	
SN	No	–	–	–	
BHs5e0.1v5	Yes	10^5	0.1	Kinetic	5000
BHs6e0.1v5	Yes	10^6	0.1	Kinetic	5000
BHs4e0.1v5	Yes	10^4	0.1	Kinetic	5000
BHs5e1v5	Yes	10^5	1	Kinetic	5000
BHs5e0v5	Yes	10^5	0	Kinetic	5000
BHs5e0.1v10	Yes	10^5	0.1	Kinetic	10000
BHs5e0.1v1	Yes	10^5	0.1	Kinetic	1000
BHs5e0.1TRML	Yes	10^5	0.1	Thermal	–

Here ϵ_r is the radiative efficiency, and ϵ_f is the feedback efficiency. We adopt $\epsilon_r = 0.1$, which assumes radiatively efficient accretion onto a Schwarzschild BH (Shakura & Sunyaev 1973).

Kinetic BH feedback is included (Barai et al. 2014, 2016), where the neighboring gas is pushed outward with a velocity v_w and mass outflow rate $\dot{M}_w$. Using the conservation of energy, $\frac{1}{2}\dot{M}_w v_w^2 = \dot{E}_{\rm feed}$, and Eq. (5), the BH kinetic outflow rate can be written as,

$$\dot{M}_w = 2\epsilon_f \epsilon_r \dot{M}_{\rm BH} \frac{c^2}{v_w^2}. \quad (6)$$

We use the values: $\epsilon_f = 0.05$, and $v_w = 5000$ km/s.

The BH kinetic feedback energy is distributed to the gas within a distance $h_{\rm BH}$ from the BH. A bi-cone volume is defined around the BH, of slant height $h_{\rm BH}$ and half-opening angle 45°. The cone-axis direction is randomly assigned during a BH seeding, and remains fixed henceforth for each BH. The total gas mass within the bi-cone $M_{\rm gas}^{\rm vicinity}$ is computed. A probability is calculated for the i'th gas particle inside the bi-cone, in a timestep Δt:

$$p_i = \frac{\dot{M}_w \Delta t}{M_{\rm gas}^{\rm vicinity}}, \quad (7)$$

where $\dot{M}_w$ is the mass outflow rate obtained from Eq. (6). A random number x_i is drawn uniformly distributed in the interval $[0, 1]$. If $x_i < p_i$, then the gas particle is imparted a velocity boost by AGN wind, such that:

$$\boldsymbol{v}_{\rm new} = \boldsymbol{v}_{\rm old} + v_w \hat{\boldsymbol{n}}. \quad (8)$$

The AGN wind direction $\hat{n}$ is considered radially outward from the BH.

We do not incorporate any scheme for BH *pinning*. Each BH is not repositioned at each time-step to the location of the minimum gravitational potential of its host galaxy.

We consider that when galaxies merge during hierarchical structure assembly, their hosted central BHs merge as well. In the numerical algorithm, two BH particles are allowed to merge to form a single BH, when the distance between them is smaller than the smoothing length of either one and their relative velocity is below the local sound speed (e.g., Sijacki et al. 2007; Di Matteo et al. 2012). The final merged BH has a mass equal to the sum of the BH masses, and a velocity along the center of mass of the initial two merging BHs. To impart kinetic feedback energy, the merged BH retains the bi-cone axis direction of the more massive initial BH.

2.3. Simulations

We perform cosmological hydrodynamical simulations of $(50\ {\rm Mpc})^3$ comoving volumes. Our standard resolution is eight simulations using 256^3 dark matter and 256^3 gas particles in the initial condition. The dark matter particle mass is $m_{\rm DM} = 2.47 \times 10^8 M_\odot$, and the gas particle mass is $m_{\rm gas} = 4.61 \times 10^7 M_\odot$. The gravitational softening length is set as $L_{\rm soft} = 3.3$ kpc comoving. The MUSIC[1] software (Hahn & Abel 2011) is used to generate the initial condition at $z = 100$. The concordance flat ΛCDM cosmological model is used: $\Omega_{M,0} = 0.3089, \Omega_{\Lambda,0} = 0.6911, \Omega_{B,0} = 0.0486, H_0 = 67.74$ km s^{-1} Mpc^{-1} (Ade et al. 2016, results XIII). Starting from $z = 100$, the boxes are subsequently evolved up to $z = 0$, with periodic boundary conditions.

We execute a series of simulations, with characteristics listed in Table 1. All the runs incorporate metal cooling, chemical enrichment, and SF. The first run *SFonly* has no SN feedback neither BHs, SN feedback is additionally included in the second run, while the remaining runs additionally include BHs.

- *SN* : no BH present. This is a control simulation in which only cooling, star-formation, chemical evolution, and stellar/SN feedback are implemented.
- *BHsXeYvZ* : with BH accretion and feedback. The symbols X, Y and Z indicate the parameters being varied between the simulations in the following way, $M_{\rm BHseed} = 10^X M_\odot$, BH feedback efficiency $\epsilon_f = Y$, and BH kinetic feedback kick velocity $v_w = Z \times 1000$ km/s.

Halos are identified by executing a *Friends-of-Friends* (FOF) group finder on-the-fly within our simulations. Galaxies are tracked using the subhalo finder *SubFind*, which associates substructures to FOF halos. The centre of each galaxy is considered as the location of the gravitational potential minimum of its subhalo. The halo mass ($M_{\rm halo}$) of a galaxy, and its virial radius in comoving coordinates (R_{200}), are related such that R_{200} encloses a density 200 times the mean comoving matter density of the Universe:

$$M_{\rm halo} = \frac{4\pi}{3} R_{200}^3 \left(200 \rho_{\rm crit} \Omega_{M,0}\right), \quad (9)$$

where $\rho_{\rm crit} = 3H_0^2/(8\pi G)$ is the present critical density. The galaxy stellar mass is considered as the mass of all star particles inside the subhalos obtained by the subhalo finder *SubFind*.

[1] MUSIC - Multi-scale Initial Conditions for Cosmological Simulations: https://bitbucket.org/ohahn/music

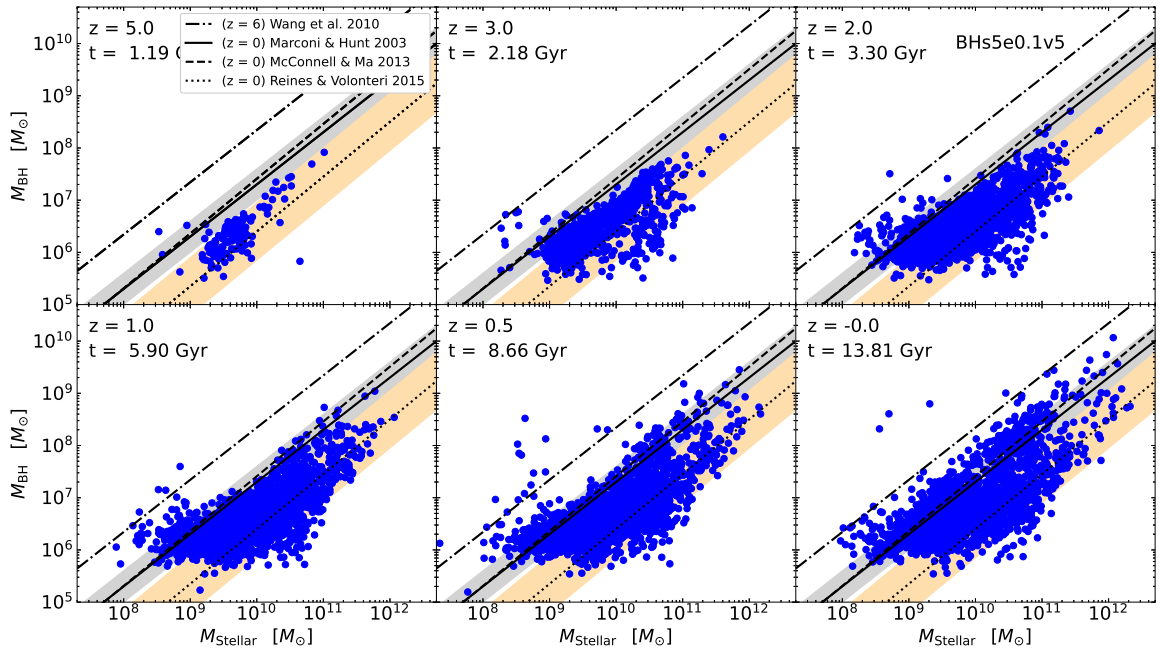

Fig. 1: Cosmic build-up of the BH mass versus stellar mass of our simulated galaxies in run *BHs5e0.1v5*, each panel indicating one redshift $z = 5, 3, 2, 1, 0.5, 0$. The blue circles are galaxies from our simulation. The black lines indicate the observed BH mass versus galaxy stellar mass relation for: local galaxies showing the correlation with the bulge mass as the solid (Marconi & Hunt 2003), dashed (McConnell & Ma 2013), and dotted (Reines & Volonteri 2015) lines; as well as $z \sim 6$ quasars (Wang et al. 2010) as the dash-dotted line.

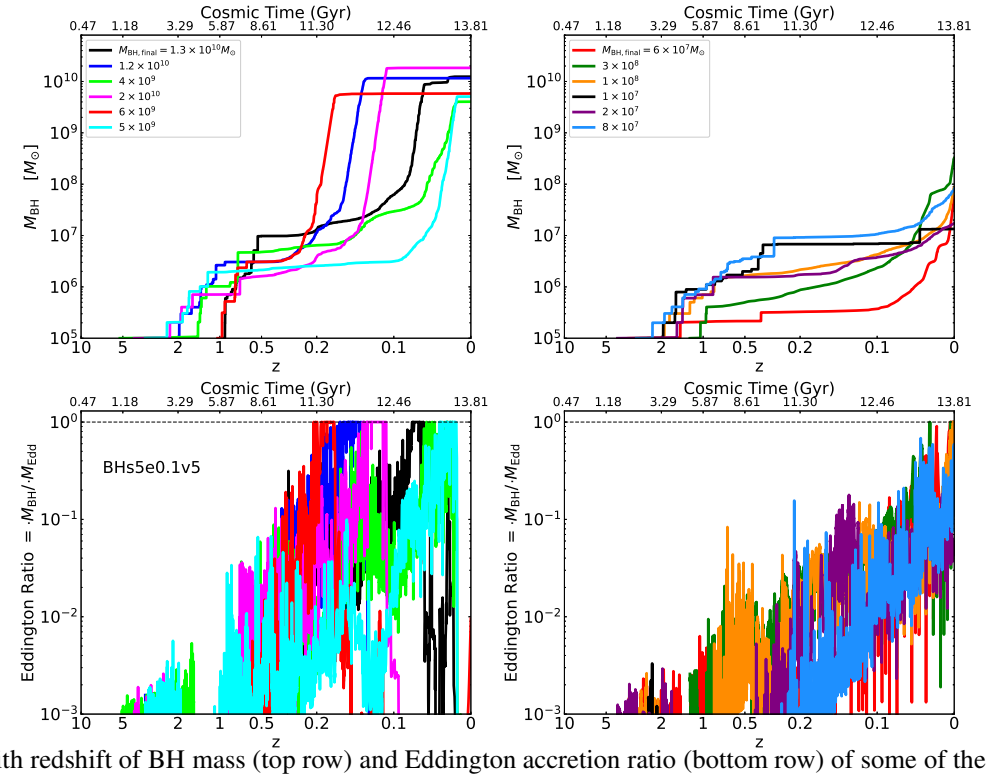

Fig. 2: Growth with redshift of BH mass (top row) and Eddington accretion ratio (bottom row) of some of the massive BHs in our standard simulation *BHs5e0.1v5*. The left column indicate six most-massive BHs with final mass $M_{BH(z=0)} > 10^9 M_\odot$, and the right column shows six intermediate-mass BHs of $M_{BH(z=0)} = (10^7 - 10^8) M_\odot$.

3. Results and Discussion

3.1. $M_{\rm BH}$ vs. $M_\star$ Relation Build-Up with Cosmic Time

The cosmic build-up of the BH mass $M_{\rm BH}$ versus stellar mass $M_\star$ of our simulated galaxies is shown in Fig. 1. Six epochs are plotted of our standard run *BHs5e0.1v5* (which gives the best-fit to the observational Marconi & Hunt (2003) $z = 0$ correlation), one each at $z = 5, 3, 2, 1, 0.5, 0$. Observational data is overplotted as the black lines indicating the BH mass versus stellar bulge mass relationships at different epochs. Local galaxies ($z = 0$) are represented by the solid line: $M_{\rm BH}/M_\star = 0.002$ (Marconi & Hunt 2003), as well as from Reines & Volonteri (2015) as the dotted line, and from McConnell & Ma (2013) as the dashed line. The ratio is observed to be steeper at high-z. Bright $z \sim 6$ quasars, observed in the far-IR and CO, lie along the dash-dotted line: median $M_{\rm BH}/M_\star = 0.022$ (Wang et al. 2010).

We find the slope of the $[M_{\rm BH} - M_\star]$ correlation remains almost constant in our simulations, and there is an intercept evolution with cosmic time. Noting that the observational relation by Reines & Volonteri (2015) lies somewhat lower than that by Marconi & Hunt (2003) and McConnell & Ma (2013); consequently our simulated galaxies are found to follow these different relations at distinct redshifts. At earlier epochs $z = 5, 3$ the BHs follow more closely the Reines & Volonteri (2015) correlation, at $z = 2 - 1$ the BHs are in between the two relations, while at current epochs $z = 0$ they lie more on the Marconi & Hunt (2003) and McConnell & Ma (2013) correlations.

3.2. Mass Growth of the Supermassive Black Holes: Merger-driven versus Accretion-driven Regimes

In our simulations, the first BHs are seeded at $z \sim 9$. Generally in such cosmological simulations, the redshift of the seeding of BHs is a quantity dependent on periodic boxsize and numerical resolution. For our standard resolution runs, $z = 8.5-9$ is the first epoch when a massive halo reach $M_{\rm halo} = 10^{10} M_\odot$; henceforth a BH of $10^5 M_\odot$ is seeded at its center. More BHs are seeded at later epochs following the prescription described in the methods.

We find that none of the first seeds (those BHs that are seeded at $z \sim 9$) grow to become one of the most-massive BHs at $z = 0$. The BHs which become most-massive are actually seeded at later epochs $z \sim 2-5$. This is because of the different BH growth modes, as described next.

The growth with redshift of some of the massive BHs in our *BHs5e0.1v5* run is plotted in Fig. 2: BH mass in the top row, and Eddington accretion ratio = $\dot{M}_{\rm BH}/\dot{M}_{\rm Edd}$ in the bottom row. Each BH starts from an initial seed of $M_{\rm BH} = 10^5 M_\odot$. The subsequent mass growth is due to merger with other BHs (revealed as vertical rises in $M_{\rm BH}$), and gas accretion (visualized as the positive-sloped regions of the $M_{\rm BH}$ versus z curve).

We quantify the driving mechanism of the mass growth of the BHs using a limiting Eddington accretion ratio of 0.1. If $\dot{M}_{\rm BH}/\dot{M}_{\rm Edd} \geq 0.1$ then it is considered as an Accretion-driven mass growth regime; while $\dot{M}_{\rm BH}/\dot{M}_{\rm Edd} < 0.1$ is considered as a Merger-Driven growth regime. The results of these two growth regimes are plotted in Fig. 3. The left column shows the mass growth due to mergers with other BHs and the right column presents the mass growth due to gas accretion, of six most-massive BHs (top row) and six intermediate-mass BHs (bottom row) from our standard simulation *BHs5e0.1v5* (the same BHs as plotted in Fig. 2).

We find that the initial growth from $10^5 M_\odot$ seeds to $\sim 10^7 M_\odot$ occurs predominantly via BH mergers (left two panels of Fig. 3). For the BHs that become supermassive with mass $\geq 10^9 M_\odot$, their final growth occurs over a period of 600 − 700 Myr dominated by efficient gas accretion (top-right panel of Fig. 3). This period corresponds to an Eddington-limited accretion where Eddington ratio = 1 (bottom-left panel of Fig. 2). During this period, the BH mass increases by a factor $10^2 - 10^3$; which grows the BHs from $10^7 M_\odot$ to $(10^9 - 10^{10}) M_\odot$ in a short time of 600 − 700 Myr. After this point, the SMBHs have a flat mass evolution with redshift (top-left panel of Fig. 3), i.e. they stop growing up to $z = 0$. We speculate this final growth halt happens because of gas depletion from galaxy centers.

The cosmic epoch of this rapid efficient gas accretion is also seen to vary depending on the SMBH, as can be seen in the top-right panel of Fig. 3. E.g., the red curve grows from $M_{\rm BH} = 7 \times 10^6 M_\odot$ at $z = 0.4$ to $M_{\rm BH} = 6 \times 10^9 M_\odot$ at $z \sim 0.3$ and has a passive evolution thereafter. While the cyan curve grows from $M_{\rm BH} = 4 \times 10^6 M_\odot$ at $z = 0.1$ to $M_{\rm BH} = 5 \times 10^9 M_\odot$ at $z = 0.05$. The consistent feature among all the BHs is that the final growth inevitably happens within a period of 600 − 700 Myr (as described in the previous paragraph).

We argue the physical reason behind such BH growth behavior is the influence of gas supply to the host galaxy center, and subsequent efficient gas accretion onto the BH, leading to gas depletion within 700 Myr.

The right column of Fig. 2 and the bottom row of Fig. 3 presents six intermediate-mass BHs: those which reach $M_{\rm BH(z=0)} = (10^7 - 10^8) M_\odot$ at the present epoch. We find that their growth have happened primarily via BH mergers (indicated by vertical rises of $M_{\rm BH}$). Their accretion ratio remains sub-Eddington. At $z < 0.05$, some of them (blue, green, red, orange curves) reach Eddington ratio = 1 for 100 − 200 Myr, but soon becomes sub-Eddington because of gas depletion.

3.2.1. Implications for the Little Red Dots

We can apply our numerical simulation results of SMBH growth to the $z > 4$ little-red-dots recently observed by JWST (e.g., Labbé et al. 2023; Killi et al. 2024; Matthee et al. 2024): sources with a compact morphology, red optical color having a V-shaped spectral energy distribution, and spectroscopic broad Balmer emission lines. The observed emission of the little-red-dots likely consist of an AGN component (e.g., Greene et al. 2024; Xiao et al. 2025) with BH mass in the range $M_{\rm BH} = 10^6 - 10^8 M_\odot$, and/or a compact starburst (e.g., Pérez-González et al. 2024; Williams et al. 2024).

With the AGN source interpretation, the little-red-dots represent low-luminosity AGN (e.g., Ma et al. 2025); which are often obscured by dust (e.g., Fujimoto et al. 2022; Akins et al. 2023) in the early Universe. These high-z faint AGN comprise of a surprisingly abundant population at $z > 5$; with a volume number density ~ 100 times the extrapolated quasar UV luminosity function (e.g., Matthee et al. 2024; Lin et al. 2024). As a fraction of the galaxy population, Harikane et al. (2023) found that $\sim 5\%$ of galaxies at $z = 4 - 7$ are type-1 AGN with broad lines, which is thus a higher fraction than $z \sim 0$ galaxies with similar luminosities.

When the host galaxy stellar masses of the little-red-dots are inferred from observations, and compared to the local $[M_{\rm BH} - M_\star]$ correlation, it implies a fast black hole growth at early epochs (Harikane et al. 2023). Interpreting with our numerical simulation results on the growth modes of the BHs presented §3.2: the high-z BH growth observed in studies like (Harikane et al. 2023) must have been dominated by efficient gas accretion.

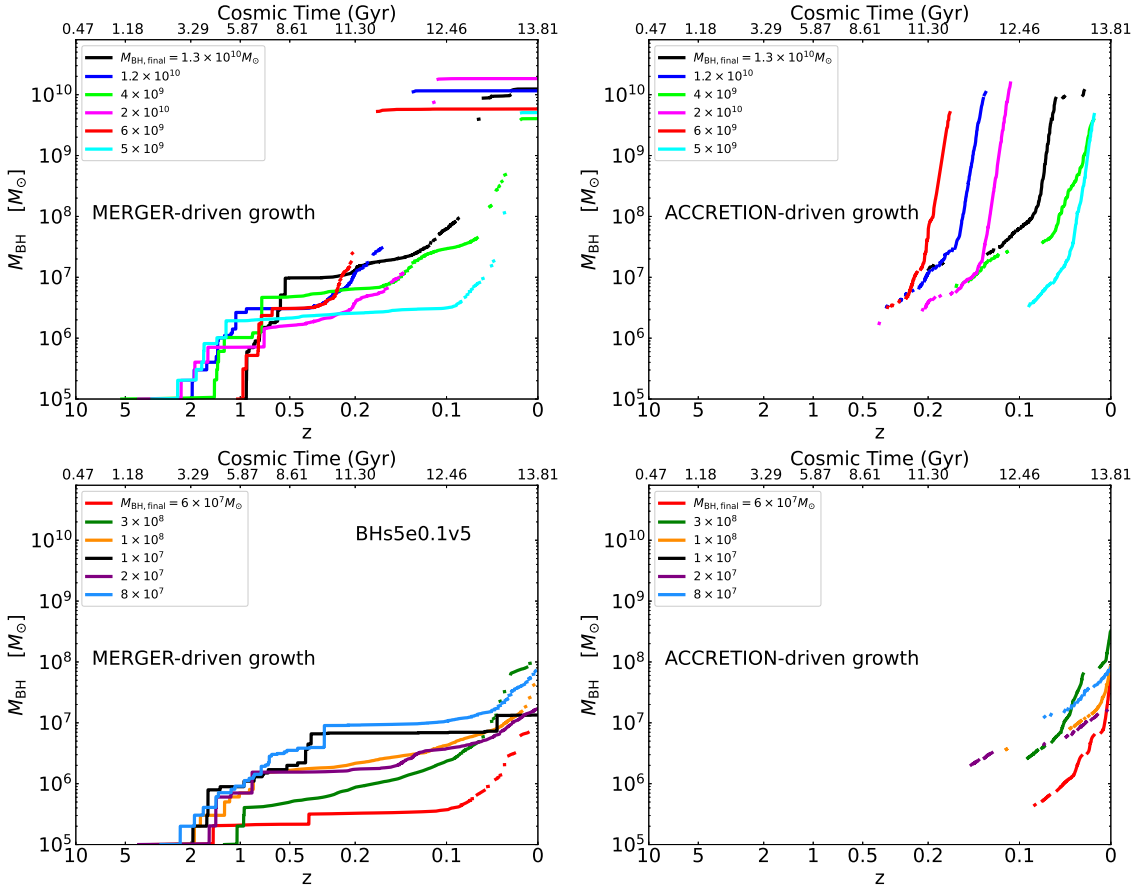

Fig. 3: Growth of BH mass due to Mergers or Accretion of the same BHs as plotted in Fig. 2: six most-massive BHs (top row) and six intermediate-mass BHs (bottom row) from our standard simulation *BHs5e0.1v5*. The left column shows the Merger-Dominated mass growth regime and the right column presents the Accretion-Dominated mass growth regime; the two regimes distinguished with a limiting Eddington accretion ratio = 0.1 as described in §3.2.

Our implications of the little-red-dots assumes the AGN source interpretation. These JWST-detected early SMBHs at $z \sim 4-12$ comprise of some BHs which are overmassive (e.g., Goulding et al. 2023; Wu et al. 2025) in their host galaxy, as well as some normal-mass SMBHs (e.g., Li et al. 2025; Geris et al. 2025) with respect to the local $M_{\rm BH} - M_\star$ correlation. Applying our results to these high-z AGN in Little Red Dots, we assert that: the normal-mass SMBHs had predominantly undergone BH merger driven evolution, whereas the overmassive BHs underwent periods of Eddington-limited or super-Eddington bursts of efficient gas accretion. The high nuclear gas density in the galaxies forming in the early Universe lead to effective gas accretion onto BHs turning them overmassive. These trends also imply that the $[M_{\rm BH} - M_\star]$ relation becomes more defined (i.e. with a smaller scatter) at lower redshifts.

3.3. Cosmic Evolution along the $[M_{\rm BH} - M_\star]$ diagram

The right panels of Fig. 4 show the evolution track with cosmic time of the BH mass versus host galaxy stellar mass of the six most-massive BHs (top row) and six intermediate-mass BHs (bottom row); these are same BHs which were plotted in Fig. 2. The corresponding redshift evolution of the host galaxy stellar mass of each BH is shown in the left panels of Fig. 4. We can visualize (top-left panel) that each SMBH mostly stay in the same host galaxy which builds up with time, and might undergo merger to form a larger galaxy, when the stellar mass increases sharply. There can be occasions when the BH migrates to a less-massive host galaxy, for a short period of time, which happens with *bh*6 (the cyan curve) at $z \sim 1.8$.

The temporary migration of a BH from a more-massive host galaxy to a less-massive galaxy happens much more frequently with the IMBHs (bottom-left panel); *bh*8, *bh*9, *bh*10, and *bh*12, demonstrate such migration signatures when the stellar mass decreases abruptly for some time. Such host migration happens more frequently for the IMBHs as compared to the SMBHs because of a greater influence of dynamical forces.

In the right panels of Fig. 4, each track starts at a point in the bottom-left which corresponds to an epoch when the BH was seeded $z \sim 3-5$, and evolve up to the top-right point $z = 0$. After seeding, the BHs start below the observed $[M_{\rm BH} - M_\star]$ correlation, and they slowly evolve to the $z = 0$ correlation first, and some BHs eventually toward the $z = 6$ correlation. The SMBHs (top-right panel) has reached the observed correlation at $z = 0$. While the IMBHs (bottom-right panel) still lies below the observed correlation.

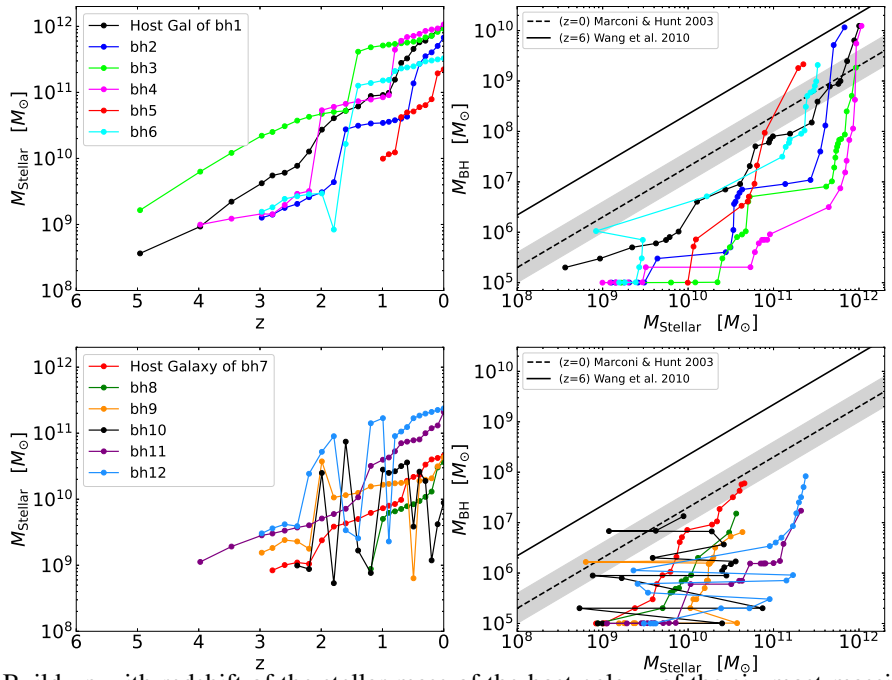

Fig. 4: Left column: Build up with redshift of the stellar mass of the host galaxy of the six most-massive BHs (top row) and six intermediate-mass BHs (bottom row); same BHs which were plotted in Fig. 2, distinguished by the plotting colours. Right column: Redshift track or the evolution with cosmic time of the BH mass versus host galaxy stellar mass of the black holes. The black lines indicate the observed BH mass versus galaxy stellar mass relation of: local galaxies (Marconi & Hunt 2003) as the dashed line, and $z = 6$ quasars (Wang et al. 2010) as the solid line.

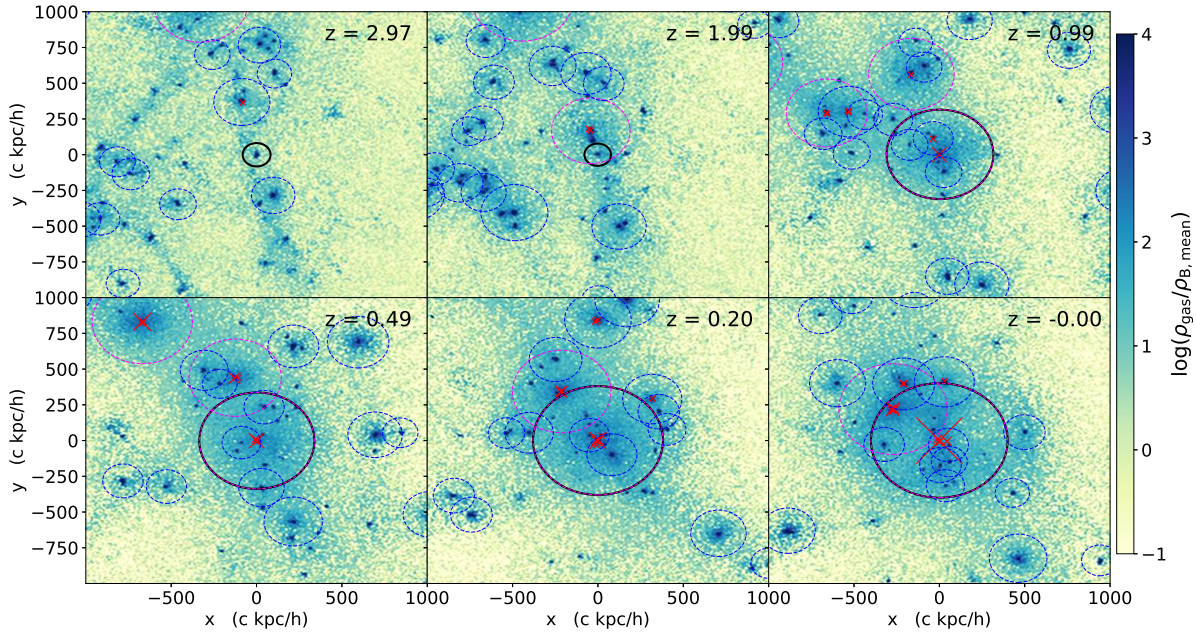

Fig. 5: Gas overdensity in our standard simulation *BHs5e0.1v5* at six epochs $z = 3, 2, 1, 0.5, 0.2, 0$. The BH which would become most-massive at $z = 0$ is back tracked, and each panel shows a projected $(2000h^{-1}$ kpc$)^3$ comoving volume around the location of this BH. The red cross symbols indicate the positions of all the BHs inside the plotted region, with the symbol size proportional to BH mass. The black circle is the virial radius R_{200} of the host galaxy of the back-tracked BH, the red circles depict the R_{200} of the galaxies with the mass range $M_{halo} > 10^{12} M_\odot$, while the blue circles show the R_{200} of $(10^{11} < M_{halo} < 10^{12}) M_\odot$ galaxies.

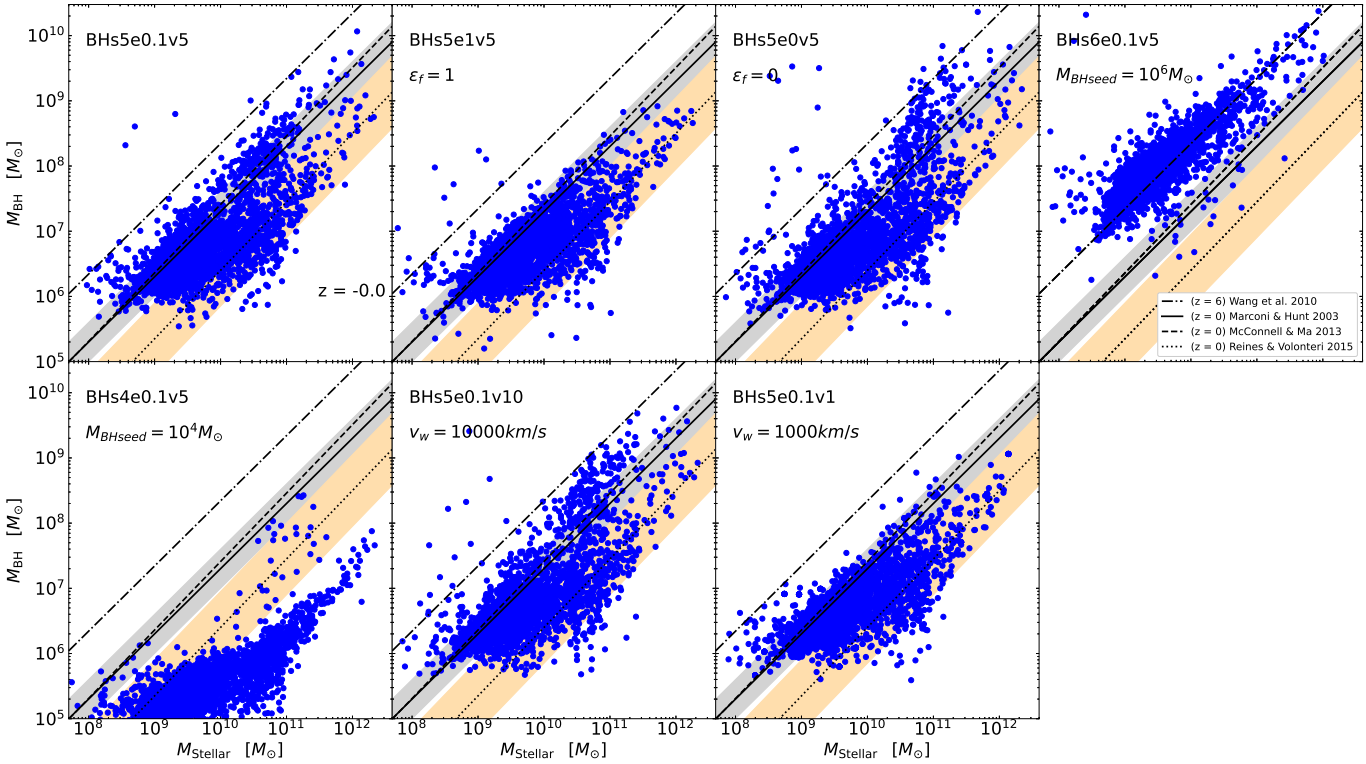

Fig. 6: BH mass versus stellar mass of the galaxies obtained in our simulations, at the current epoch $z = 0$, each panel indicating one distinct run. The black lines indicate the observed BH mass versus galaxy stellar mass relation for: local galaxies showing the correlation with the bulge mass as the solid (Marconi & Hunt 2003), dashed (McConnell & Ma 2013), and dotted (Reines & Volonteri 2015) lines; as well as $z \sim 6$ quasars (Wang et al. 2010) as the dash-dotted line.

3.4. Environment of the BHs

The evolution of gas environment around an assembling massive BH is plotted in Fig. 5. It displays gas overdensity (i.e., the ratio between the gas density and the cosmological mean baryon density of the Universe) in our simulation *BHs5e0.1v5*, at six epochs $z = 3, 2, 1, 0.5, 0.2, 0$. The BH which would become most-massive in this run at $z = 0$ is back tracked, and each panel shows a projected $(2000h^{-1}$ kpc$)^3$ comoving volume around the location of this BH. The black circle is the virial radius R_{200} (defined in Eq. 9) of the host galaxy of the back-tracked BH, the red circles depict the R_{200} of the galaxies with the mass range $M_{\rm halo} > 10^{12} M_\odot$, while the blue circles show the R_{200} of $(10^{11} < M_{\rm halo} < 10^{12}) M_\odot$ galaxies. The spatial locations of all the BHs inside the plotted region can be visualized with the red cross symbols, with the symbol size proportional to BH mass.

In the top panels of Fig. 5 we can see the cosmological large-scale-structure Mpc-scale filaments, consisting of dense (blue and dark-blue regions) gas. The galaxies (blue and red circles) lie along the filaments, or at the high-density intersections of the filaments, and finally in the galaxy cluster region which has formed at $z = 0$. The clustering of halos are visible in all the panels: at $z = 3, 2, 1$ the halos are forming along cosmological large-scale-structure filaments. While at $z = 0.5, 0.2$ the halos have formed a overdense proto-cluster region at the center of the plotted volume, which evolves to a dense galaxy cluster region at $z = 0$. Thus the most-massive BH in this simulation of $M_{\rm BH(z=0)} = 2 \times 10^{10} M_\odot$ lies at the center of a galaxy cluster.

3.5. Influence of AGN Feedback Model Parameters

The BH mass versus galaxy stellar mass correlation obtained in 7 of our simulations at the current epoch $z = 0$ is presented in Fig. 6. We find a relatively large scatter in the $[M_{\rm BH} - M_\star]$ correlation of our simulated galaxies, which is comparable to the scatter found in observations (e.g., Reines & Volonteri 2015). Our standard simulation *BHs5e0.1v5* with $M_{\rm BHseed} = 10^5 M_\odot$, $\epsilon_f = 0.1$ and $v_w = 5000$ km/s; is able to well reproduce the observational (Marconi & Hunt 2003) $z = 0$ correlation.

Among the relevant BH subgrid model parameter variations, the largest impact is seen with the BH seed mass. With a higher $M_{\rm BHseed} = 10^6 M_\odot$ (run *BHs6e0.1v5*), the resulting BHs are too massive and overshoot the local relation. On seeding with a lower seed mass of $M_{\rm BHseed} = 10^4 M_\odot$ (run *BHs4e0.1v5*), the resulting BHs do not grow enough and remain below the local one. There is a relatively lower impact of the BH feedback efficiency and the feedback kick velocity. With $\epsilon_f = 1$ (run *BHs5e1v5*) and with $v_w = 1000$ km/s (run *BHs5e0.1v1*) the BHs lie slightly below the local $[M_{\rm BH} - M_\star]$ correlation. With $\epsilon_f = 0$ (run *BHs5e0v5*) and with $v_w = 10000$ km/s (run *BHs5e0.1v10*) the BHs lie slightly above the $z = 0$ local relation.

Worthwhile to note that the simulation with $\epsilon_f = 0$ (run *BHs5e0v5*) is one with no BH feedback because the efficiency (viz. Eq. (5)) is set to zero, as a test case. From the top row, third panel of Fig. 6, we thus find that even with no BH feedback some kind of $[M_{\rm BH} - M_\star]$ correlation is generated in the simulations.

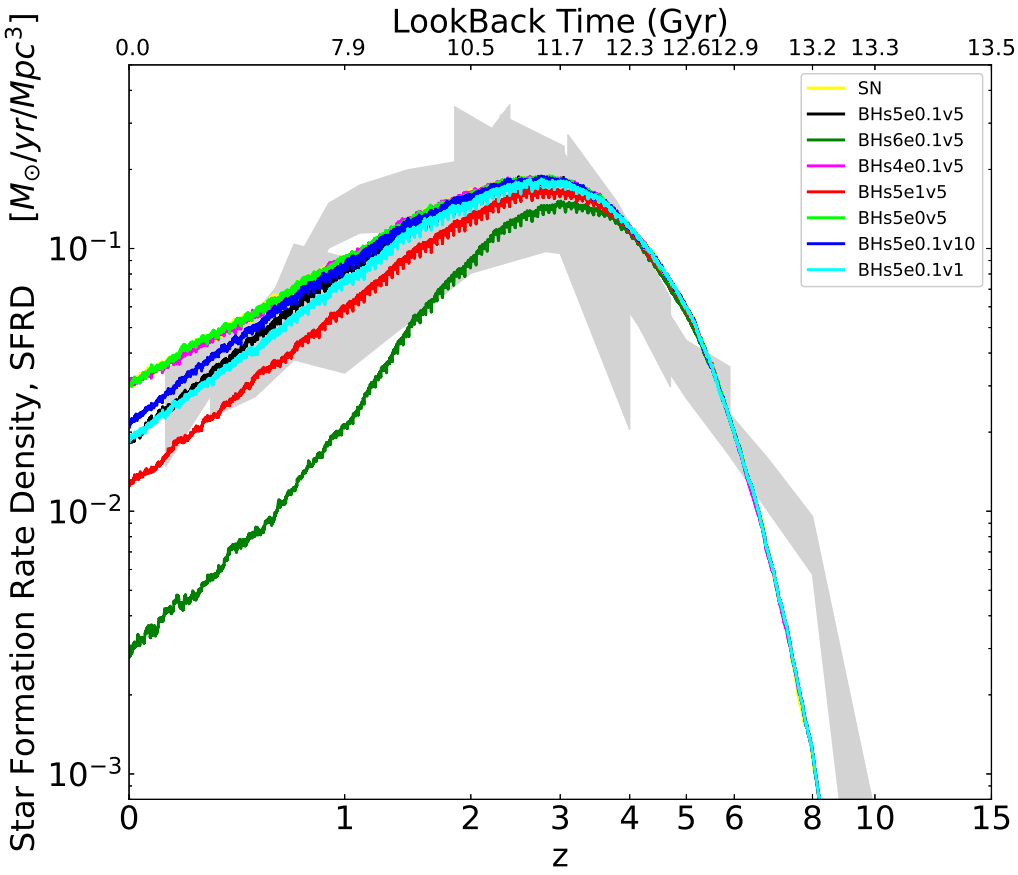

Fig. 7: Star formation rate density integrated over the whole simulation volume as a function of redshift, with the different simulation runs labelled by the colours and linestyles. The grey shaded region denotes a combination of observational SFRD data range from Cucciati et al. (2012), and the compilations therein originally from Pérez-González et al. (2005), Schiminovich et al. (2005), Bouwens et al. (2009), Reddy & Steidel (2009), Rodighiero et al. (2010), van der Burg et al. (2010), Bouwens et al. (2012).

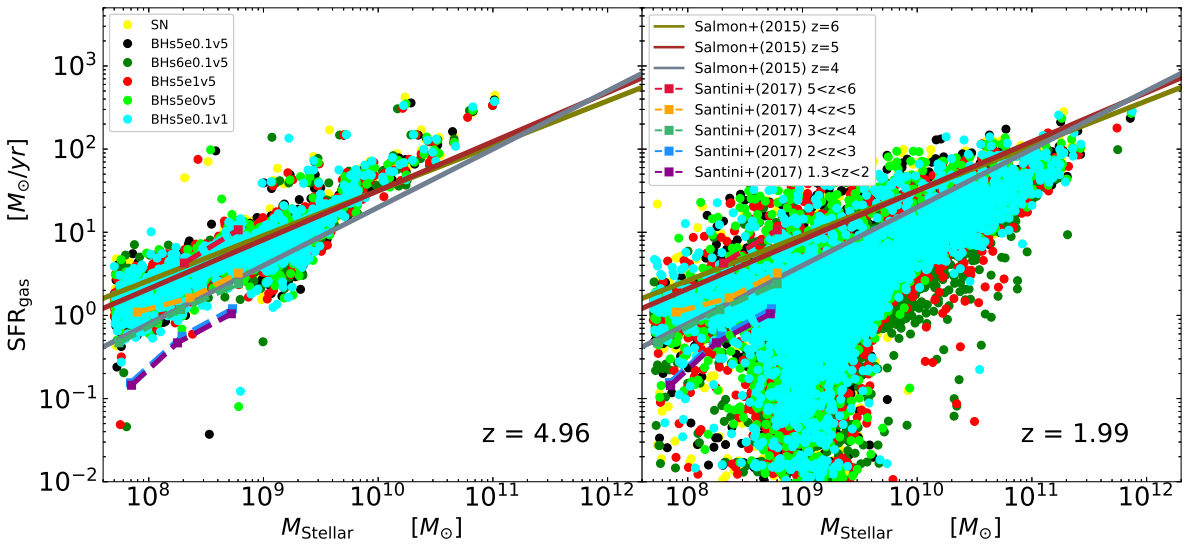

Fig. 8: SFR versus stellar mass of the galaxies in our simulations, at the epoch $z \sim 5$ in the left, and $z \sim 2$ in the right panel. The filled circles are our simulation results, and the plotting colours distinguish results from different runs. The lines indicate observational results of SFR versus stellar mass relation for: star-forming galaxies at $z = 4, 5, 6$ (Salmon et al. 2015) as the solid lines, and galaxies in different redshift bins within $z = 1.3 - 6$ (Santini et al. 2017) as the dashed lines with square plotting symbols.

3.6. Star Formation Rate

We compute the Star Formation Rate Density (SFRD) (in $M_\odot$ yr^{-1} Mpc^{-3}) by summing over all the SF occurring in each simulation box at a time, and dividing it by the time-step interval and the box volume. The global SFRD as a function of redshift is presented in Fig. 7, the eight simulations labelled by the different colours. Observational data limits are shown, for a comparison, as the grey shaded region, taken mainly from Cucciati et al. (2012), and the compilations therein originally from Pérez-González et al. (2005), Schiminovich et al. (2005), Bouwens et al. (2009), Reddy & Steidel (2009), Rodighiero et al. (2010), van der Burg et al. (2010), Bouwens et al. (2012). The SFRD from these observations continues to grow from early cosmic epochs at $z < 10$, and has a peak around $z \sim 2-3$.

In our simulations we find that the SFRD rises with time from early epochs $z \sim 10$, reach a maximum SFRD in the form of a wide peak at $z \sim 2-3$, and the SFRD decreases at $z < 3$; an overall trend consistent with the observations. Star formation occurs inside galaxies, where cosmic large-scale-structure gas inflows and cools. The presence of a central SMBH helps to quench SF, because a fraction of gas is ejected out and/or heated by BH feedback, and a small fraction might be accreted onto the BH.

We consider the *SN* run (yellow curve) without BHs as the baseline, and compare other simulations with it to estimate the impact of BH feedback. Note that in the run *BHs5e0v5* (light green curve) no BH feedback is implemented, or $\epsilon_f = 0$; and here the SF remains the same as the *SN* run. However growth of the BHs by gas accretion and mergers is present. Thus we conclude that gas removal by accretion onto BHs play only a very minor role in suppressing SF, and the major role is played by BH feedback induced removal/heating of gas.

We find that the physical processes of BH accretion and feedback causes a quenching of the SFRD compared to the *SN* case (yellow curve in Fig. 7), at cosmic epochs $z \leq 4$. The reduction of SFRD factors at $z = 0$ for the different simulations range between 1.3 – 15 times.

To explore the galaxy main-sequence, we plot the SFR (in $M_\odot/yr$) versus stellar mass ($M_\star$) of all the galaxies within the cosmological boxes in Fig. 8; at the epoch $z \sim 5$ in the left panel, and $z \sim 2$ at the right. The filled circles are our simulation results, with the plotting colours distinguishing results from different runs. The solid lines indicate observational data from Salmon et al. (2015) of star-forming galaxies at $z = 4, 5, 6$: the best-fit relation of SFR versus $M_\star$ as written in their Equation (6) with parameters given in their Table 4. The dashed lines show observations from Santini et al. (2017) in different redshift bins within $z = 1.3-6$: the data points are taken from their Table 1.

We find that our simulated galaxies are well consistent with the [SFR $-M_\star$] relations showing the observational main sequence of star-forming galaxies. There is however a large scatter in our SFR versus $M_\star$ correlation.

4. Summary and Conclusions

How the central supermassive black holes grew to billions of solar masses and produced the varied populations of AGN that we observe, involves unresolved questions. Especially at early epochs, luminous $z \sim 6$ quasars are observed to host $10^9 M_\odot$ SMBHs when the Universe was < 1 Gyr old. It is challenging to understand how they formed over such short time-scales, with varying possible theories: growth from stellar-mass seed BHs by rapid enhanced super-Eddington accretion, formation of direct-collapse heavy $10^5 M_\odot$ BH seeds soon after the Big Bang, or via mergers of intermediate-mass black holes.

Adding to the population of early SMBHs, recent JWST observations are detecting many SMBHs at $z \sim 4-12$ which are overmassive in their host galaxy, as well as some SMBHs which are normal-mass with respect to the local $M_{\rm BH} - M_\star$ correlation. The exact formation channels of these diverse populations of normal-mass and overmassive SMBHs are unknown.

We have investigated the growth of SMBHs versus host galaxies, as well as their feedback, by performing cosmological hydrodynamical simulations. Using a modified version of the SPH code GADGET-3, we simulated (50 Mpc)^3 comoving volumes, with a mass resolution of $4.61 \times 10^7 M_\odot$ for gas particles, from $z = 100$ up to $z = 0$. The simulations include the sub-resolution physics of radiative cooling, star-formation, stellar evolution, chemical enrichment, SN feedback, AGN accretion and feedback. We probe the BH-galaxy co-evolution in terms of the black hole mass - stellar mass correlation.

We executed a series of simulations: two of them are control cases; one with SF-only and one additionally SN feedback; the other runs include BHs as well. We explore different parameter variations of the BH sub-resolution models: $M_{\rm BHseed} = (10^4, 10^5, 10^6) M_\odot$, $\epsilon_f = 0, 0.1, 1$, the outflow velocity for BH kinetic feedback: $v_w = 1000, 5000, 10000$ km/s.

Based on our simulations, in our study we find the following:

- The initial growth from $10^5 M_\odot$ seeds to $\sim 10^7 M_\odot$ BHs occurs predominantly via BH mergers.
- Gas accretion onto the BHs is initially low, with highly sub-Eddington accretion rates ($\dot{M}_{\rm BH}/\dot{M}_{\rm Edd} < 0.001$). $\dot{M}_{\rm BH}$ increases with time, and reaches the Eddington rate after 7 – 9 Gyrs. The BHs then undergo very fast growth via Eddington-limited (or Eddington ratio = 1) gas accretion. Within a period of 600 – 700 Myr, the BHs grow from $10^7 M_\odot$ to $(10^9 - 10^{10}) M_\odot$.
- Supermassive BHs (those reaching $10^9 - 10^{10} M_\odot$ at $z = 0$) have had their predominant growth over a period of 600 – 700 Myr via strong gas accretion. During this period, the BH mass increases by a factor $10^2 - 10^3$. We argue that such BH growth behavior results from the influence of gas supply to the host galaxy center, and subsequent efficient gas accretion onto the BH; which leads to central gas depletion within 700 Myr.
- After the Eddington-limited gas accretion growth to $\sim 10^9 - 10^{10} M_\odot$, the SMBHs stop growing and maintains the same mass up to $z = 0$. This final growth halt happens because of gas depletion from galaxy centers.
- The most-massive population of BHs have grown to $M_{\rm BH} \sim 10^{10} M_\odot$ at $z = 0$. BHs do not grow to more than $10^{10} M_\odot$, because of gas removal by AGN feedback driven self-regulation. Some BHs may reach this maximum mass 2 or 3 Gyr ago.
- Applying our results to the JWST detected high-z Little Red Dots, we argue that: the normal-mass SMBHs had predominantly undergone BH merger driven evolution, whereas the overmassive BHs underwent periods of Eddington-limited or super-Eddington bursts of gas accretion.
- Our simulations probe galaxies with a stellar mass between $M_\star = (10^8 - 10^{12}) M_\odot$. The star formation rate density ($M_\odot$ yr^{-1} Mpc^{-3}) versus redshift evolution, as well as the main-sequence of SFR-stellar mass relation of these galaxies, are consistent with observations. Star-formation is quenched at $z = 3 - 0$, and the SFRD is reduced by factors 1.3 – 15.

– Gas removal by accretion onto BHs play only a very minor role in suppressing SF, and the major role is played by BH feedback induced removal/heating of gas.

We deduce that supermassive $10^9 - 10^{10} M_\odot$ *BHs have had their predominant growth over a period of* $600 - 700$ *Myr via efficient gas accretion, from the gas supply to the host galaxy center, when the BH mass increases* $10^2 - 10^3$ *times. BH mergers play a minor role compared to gas accretion for SMBH growth. SMBHs do not grow to more than* $10^{10} M_\odot$*, because of gas depletion from galaxy centers driven by AGN feedback.*

References

Ade, P. A., Aghanim, N., Arnaud, M., et al. 2016, A&A, 594, A13
Akins, H. B., Casey, C. M., Allen, N., et al. 2023, ApJ, 956, 61
Alexander, D. M., Hickox, R. C., Aird, J., et al. 2025, arXiv e-prints, arXiv:2506.19166
Barai, P. & de Gouveia Dal Pino, E. M. 2019, MNRAS, 487, 5549
Barai, P., Martel, H., & Germain, J. 2011, ApJ, 727, 54
Barai, P., Monaco, P., Murante, G., et al. 2015, MNRAS, 447, 266
Barai, P., Murante, G., Borgani, S., et al. 2016, MNRAS, 461, 1548
Barai, P., Viel, M., Borgani, S., et al. 2013, MNRAS, 430, 3213
Barai, P., Viel, M., Murante, G., et al. 2014, MNRAS, 437, 1456
Bhatt, M., Gallerani, S., Ferrara, A., et al. 2024, A&A, 686, A141
Biffi, V., Borgani, S., Murante, G., et al. 2016, ApJ, 827, 112
Bondi, H. 1952, MNRAS, 112, 195
Bouché, N., Hohensee, W., Vargas, R., et al. 2012, MNRAS, 426, 801
Bouwens, R., Illingworth, G., Franx, M., et al. 2009, ApJ, 705, 936
Bouwens, R. J., Illingworth, G., Oesch, P., et al. 2012, ApJ, 754, 83
Chabrier, G. 2003, PASP, 115, 763
Cucciati, O., Tresse, L., Ilbert, O., et al. 2012, A&A, 539, A31
Di Matteo, T., Khandai, N., DeGraf, C., et al. 2012, ApJ, 745, L29
Di Matteo, T., Springel, V., & Hernquist, L. 2005, Nature, 433, 604
Dijkstra, M., Haiman, Z., Mesinger, A., et al. 2008, MNRAS, 391, 1961
Dubois, Y., Peirani, S., Pichon, C., et al. 2016, MNRAS, 463, 3948
Dubois, Y., Pichon, C., Devriendt, J., et al. 2013, MNRAS, 428, 2885
Fan, X., Bañados, E., & Simcoe, R. A. 2023, ARA&A, 61, 373
Ferland, G., Korista, K., Verner, D., et al. 1998, PASP, 110, 761
Fontanot, F., De Lucia, G., Hirschmann, M., et al. 2020, MNRAS, 496, 3943
Fujimoto, S., Brammer, G. B., Watson, D., et al. 2022, Nature, 604, 261
Geris, S., Maiolino, R., Isobe, Y., et al. 2025, arXiv e-prints, arXiv:2506.22147
Goulding, A. D., Greene, J. E., Setton, D. J., et al. 2023, ApJ, 955, L24
Graham, A. W., Chilingarian, I. V., Nguyen, D. D., et al. 2025, arXiv e-prints, arXiv:2503.10958
Greene, J. E., Labbe, I., Goulding, A. D., et al. 2024, ApJ, 964, 39
Haardt, F. & Madau, P. 2001, in Clusters of Galaxies and the High Redshift Universe Observed in X-rays, ed. D. M. Neumann & J. T. V. Tran, 64
Habouzit, M., Onoue, M., Bañados, E., et al. 2022, MNRAS, 511, 3751
Hahn, O. & Abel, T. 2011, MNRAS, 415, 2101
Haidar, H., Habouzit, M., Volonteri, M., et al. 2022, MNRAS, 514, 4912
Harikane, Y., Zhang, Y., Nakajima, K., et al. 2023, ApJ, 959, 39
Inayoshi, K. & Omukai, K. 2012, MNRAS, 422, 2539
Jeon, J., Liu, B., Taylor, A. J., et al. 2025, arXiv e-prints, arXiv:2503.14703
Johansson, P. H., Naab, T., & Burkert, A. 2008, ApJ, 690, 802
Juodzbalis, I., Maiolino, R., Baker, W. M., et al. 2025, arXiv e-prints, arXiv:2504.03551
Kauffmann, G. & Haehnelt, M. 2000, MNRAS, 311, 576
Khandai, N., Di Matteo, T., Croft, R., et al. 2015, MNRAS, 450, 1349
Kho, J., Bhowmick, A. K., Torrey, P., et al. 2025, arXiv e-prints, arXiv:2506.17476
Killi, M., Watson, D., Brammer, G., et al. 2024, A&A, 691, A52
Kocevski, D. D., Finkelstein, S. L., Barro, G., et al. 2025, ApJ, 986, 126
Kokorev, V., Fujimoto, S., Labbe, I., et al. 2023, ApJ, 957, L7
Labbé, I., van Dokkum, P., Nelson, E., et al. 2023, Nature, 616, 266
Li, J., Shen, Y., & Zhuang, M.-Y. 2025, arXiv e-prints, arXiv:2502.05048
Li, J., Silverman, J. D., Ding, X., et al. 2021, ApJ, 922, 142
Lin, X., Wang, F., Fan, X., et al. 2024, ApJ, 974, 147
Ma, Y., Greene, J. E., Volonteri, M., et al. 2025, arXiv e-prints, arXiv:2509.02662
Maiolino, R., Scholtz, J., Curtis-Lake, E., et al. 2024, A&A, 691, A145
Marconi, A. & Hunt, L. K. 2003, ApJ, 589, L21
Martin, C. L. 1999, ApJ, 513, 156
Matsumoto, T., Nakauchi, D., Ioka, K., et al. 2015, ApJ, 810, 64
Matthee, J., Naidu, R. P., Brammer, G., et al. 2024, ApJ, 963, 129
McConnell, N. J. & Ma, C.-P. 2013, ApJ, 764, 184
Melioli, C., de Gouveia Dal Pino, E., & Geraissate, F. 2013, MNRAS, 430, 3235
Natarajan, P., Pacucci, F., Ricarte, A., et al. 2024, ApJ, 960, L1
Ostriker, J. P., Choi, E., Ciotti, L., et al. 2010, ApJ, 722, 642
Pérez-González, P. G., Barro, G., Rieke, G. H., et al. 2024, ApJ, 968, 4
Pérez-González, P. G., Rieke, G. H., Egami, E., et al. 2005, ApJ, 630, 82
Reddy, N. A. & Steidel, C. C. 2009, ApJ, 692, 778
Rees, M. J. 1984, ARA&A, 22, 471
Reines, A. E. & Volonteri, M. 2015, ApJ, 813, 82
Rodighiero, G., Vaccari, M., Franceschini, A., et al. 2010, A&A, 515, A8
Salmon, B., Papovich, C., Finkelstein, S. L., et al. 2015, ApJ, 799, 183
Santini, P., Fontana, A., Castellano, M., et al. 2017, ApJ, 847, 76
Schiminovich, D., Ilbert, O., Arnouts, S., et al. 2005, ApJ, 619, L47
Scholtz, J., Maiolino, R., D'Eugenio, F., et al. 2025, A&A, 697, A175
Shakura, N. I. & Sunyaev, R. A. 1973, A&A, 24, 337
Sijacki, D., Springel, V., Di Matteo, T., & Hernquist, L. 2007, MNRAS, 380, 877
Somerville, R. S., Hopkins, P. F., Cox, T. J., et al. 2008, MNRAS, 391, 481
Springel, V. 2005, MNRAS, 364, 1105
Springel, V., Di Matteo, T., & Hernquist, L. 2005, MNRAS, 361, 776
Springel, V. & Hernquist, L. 2003, MNRAS, 339, 289
Tescari, E., Viel, M., D'Odorico, V., et al. 2011, MNRAS, 411, 826
Tornatore, L., Borgani, S., Dolag, K., & Matteucci, F. 2007, MNRAS, 382, 1050
Urry, C. M. & Padovani, P. 1995, PASP, 107, 803
van der Burg, R. F., Hildebrandt, H., & Erben, T. 2010, A&A, 523, A74
Volonteri, M. & Rees, M. J. 2005, ApJ, 633, 624
Wang, R., Carilli, C. L., Neri, R., et al. 2010, ApJ, 714, 699
Wiersma, R. P., Schaye, J., & Smith, B. D. 2009, MNRAS, 393, 99
Williams, C. C., Alberts, S., Ji, Z., et al. 2024, ApJ, 968, 34
Willott, C. J., McLure, R. J., & Jarvis, M. J. 2003, ApJ, 587, L15
Wu, Y., Wang, T., Liu, D., et al. 2025, arXiv e-prints, arXiv:2506.14896
Xiao, M., Oesch, P. A., Bing, L., et al. 2025, A&A, 700, A231
Yang, J., Fan, X., Gupta, A., et al. 2023, ApJS, 269, 27

5. Acknowledgements

P.B. is most grateful to Volker Springel and Klaus Dolag for allowing to use the GADGET-3 code. P.B. acknowledges useful discussions with Giuseppe Murante, Matteo Viel, Luca Tornatore, Stefano Borgani, Gian Luigi Granato, Pierluigi Monaco, Simona Gallerani, and Andrea Ferrara. The work has been supported by the Brazilian funding Agency FAPESP (grants 2016/01355-5 and 2016/22183-8); and the Italian Ministry of University and Research (MUR) Missione 4 "Istruzione e Ricerca" - Componente C2, Investimento 1.1 Fondo per il Programma Nazionale di Ricerca e Progetti di Rilevante Interesse Nazionale (PRIN), the PRIN 2022 PNRR grant under the National Recovery and Resilience Plan (PNRR): project P2022ZLW4T "Next-generation computing and data technologies to probe the cosmic metal content".